EDGE ARTICLE

Check for updates

Hammett neural networks: prediction of frontier orbital energies of tungsten–benzylidyne photoredox complexes†

Alexander M. Chang, [ID] Jessica G. Freeze [ID] and Victor S. Batista*

The successful application of Hammett parameters as input features for regressive machine learning models is demonstrated and applied to predict energies of frontier orbitals of highly reducing tungsten–benzylidyne complexes of the form W($\equiv$CArR)L$_4$X. Using a reference molecular framework and the *meta*- and *para*-substituent Hammett parameters of the ligands, the models predict energies of frontier orbitals that correlate with redox potentials. The regressive models capture the multivariate character of electron-donating trends as influenced by multiple substituents even for non-aryl ligands, harnessing the breadth of Hammett parameters in a generalized model. We find a tungsten catalyst with tetramethylethylenediamine (tmeda) equatorial ligands and axial methoxyl substituents that should attract significant experimental interest since it is predicted to be highly reducing when photoactivated with visible light. The utilization of Hammett parameters in this study presents a generalizable and compact representation for exploring the effects of ligand substitutions.

Introduction

The relationship between molecular structure and chemical reactivity is central for the design of catalytic systems. One of the most extensively investigated topics in structure–reactivity relationships has been the effect of substituents on the properties of aromatic compounds, as described by the Hammett equation:[1–3]

$$\sigma\rho = \log\left(\frac{K}{K_0}\right) = -\rho\Delta pK_a \qquad (1)$$

Eqn (1) provides a linear free energy relationship between the equilibrium or rate constants K_0 and K, for chemical reactions of unsubstituted (K_0) and substituted (K) benzoic acid derivatives, and the *meta*- and *para*-substituents.[1–3] A demonstration of this relationship to ΔG can be seen in the ESI.†[1] The *substituent constant* σ depends only on the nature and position of the substituent, determining the net electron-withdrawing or electron-donating character of that group, while ρ is the *reaction constant* that depends on the particular reaction of interest, type of molecule, and reaction conditions. Eqn (1) was initially tested by Hammett on 52 reactions,[1–3] and since then many other reactions have been successfully investigated with parameters σ and ρ tabulated for hundreds of different *meta*- and *para*-

substituents.[2] However, *ortho*-substituents or poly-substituted compounds often deviate from the linear relationship due to the non-additive character of the contributions when steric or solvent effects are important. Here, we introduce a neural network and various linear models that are capable of predicting frontier orbital energies, based on the σ Hammett parameters from literature.[1,2] The models bypass the usual limitations of the Hammett equation, including both aryl and non-aryl substitutions, allowing for the prediction of frontier orbital energies of tungsten–benzylidyne complexes (Fig. 1).
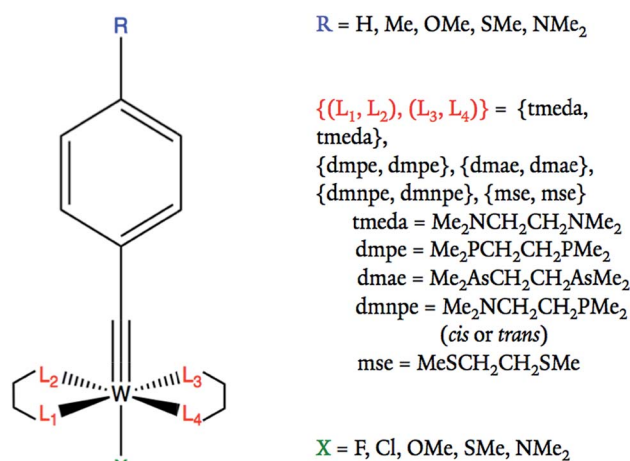

R = H, Me, OMe, SMe, NMe$_2$

{(L$_1$, L$_2$), (L$_3$, L$_4$)} = {tmeda, tmeda},
{dmpe, dmpe}, {dmae, dmae},
{dmnpe, dmnpe}, {mse, mse}
tmeda = Me$_2$NCH$_2$CH$_2$NMe$_2$
dmpe = Me$_2$PCH$_2$CH$_2$PMe$_2$
dmae = Me$_2$AsCH$_2$CH$_2$AsMe$_2$
dmnpe = Me$_2$NCH$_2$CH$_2$PMe$_2$
(*cis* or *trans*)
mse = MeSCH$_2$CH$_2$SMe

X = F, Cl, OMe, SMe, NMe$_2$

Fig. 1 Tungsten–benzylidyne molecular framework and possible substituent ligand options at each site. All R groups are in the *para* position of the benzene ring.

Department of Chemistry, Energy Sciences Institute, Yale University, New Haven, CT 06520, USA. E-mail: victor.batista@yale.edu

Tungsten–alkylidyne complexes represent a d^2 family of the photoredox chromophores of the form $W(\equiv CR')L_4X$ (R' = aryl group with organic substituent, L = neutral ligand, X = anionic ligand, where the W–X bond is *trans* to the alkylidyne ligand), with redox potentials that can be tuned over a broad range by ligand design.[4–6] In fact, Hopkins and co-workers have shown that $W(\equiv CR')L_4X$ complexes can have highly variable ligands allowing for tunable redox potentials and photophysical properties.[4,5,7] For example, 32 different $W(\equiv CR')L_4X$ compounds were synthesized and examined through variation of the R', L, and X substituents.[4] The redox active orbital of the synthesized $W(\equiv CR')L_4X$ complexes is the metal-centered d_{xy} state (typically the HOMO), with an energy level that is strongly correlated to the redox potential of the complex (Fig. 2).[4] Therefore, the ligands can be tuned to achieve highest reduction potential using the d_{xy} orbital energy as a molecular descriptor. As applications to solar photoreduction also require the energy gap d_{xy}–π^* (usually the HOMO–LUMO gap) to be in the visible range, this energy gap can be used as a molecular descriptor as well. For the purposes of this study, we focused on tungsten–benzylidyne complexes of the form $W(\equiv CArR)L_4X$ (Fig. 1), a subset of the tungsten–alkylidyne complex chemical space suggested by Hopkins and co-workers. Due to the large number of possible ligands,[8,9] high-throughput screening could be a time-consuming and computationally expensive approach. Consequently, implementing systematic methods based on inverse design may prove a more cost-effective endeavor. Inverse design, as a general concept, involves searching over a descriptor space to find a desired descriptor value and then determining the structure that matches that descriptor. Because descriptor space contains the parameter or a related parameter that one is trying to optimize, inverse design is able to perform a directed search over possible structures in contrast to the often-random ligand combinations seen in methods like high-throughput screening.

Methods based on machine learning have received prominent attention in the chemistry community, and have been used to learn patterns of a training data set and accurately predict labels such as frontier orbital energies for novel molecules,[10–16] bypassing the cost of exhaustive screening. However, incorporation of the Hammett substituent constants into these deep learning methods has not been explored. Here, we show that Hammett parameters can be used for training regressive machine learning models, varying the ligands of a given complex to render accurate quantitative descriptions. In order to determine the presence of non-linearity in the relationship between frontier orbital energies and Hammett parameter descriptors, we compare results between neural network and linear, ridge, LASSO, and stepwise regression methods, similar to the works of Sigman and co-workers.[17] The reported findings thus contribute to the emerging field of machine learning in chemistry already explored in a wide range of important directions, including force field development,[18,19] electronic structure calculations,[20,21] drug discovery,[22] new materials development,[23,24] toxicity probing,[25] prediction of chemical reactions[26] and reaction yields,[21] to mention a few.

The R, L, and X ligands are described according to their corresponding *meta-* and *para-σ* Hammett parameters, which are provided as input data for the regressive methods. The resulting models thus simultaneously account for the effects of multiple substituents, exploiting the capabilities of Hammett parameters as descriptors of electron-withdrawing/donating effects that correlate with redox potentials as well as HOMO/LUMO energies.[27–34] In fact, due to their ability to capture electron-donating trends, the substituent constants should modulate the frontier orbital energies in the d^2 $W(\equiv CArR)L_4X$ complexes, regardless of whether the corresponding ligands are aryl or not. However, the underlying correlation established by multiple Hammett constants and the frontier orbital energies has yet to be established.

In this paper, we explore the energy of the frontier orbital with predominant symmetry, d_{xy}, and the d_{xy}–π^* energy gap for a series of 150 tungsten–benzylidyne complexes. All 150 energies were calculated after geometry optimization at density functional theory (DFT) level, as implemented in Gaussian 09,[35] using the B3LYP functional[36] and the Def2SVP basis set.[37,38] The DFT energies, along with the Hammett parameters of the various substituent ligands, were then used to train and test linear and non-linear regressive models. The models were parameterized to predict the energies of the frontier orbitals from just the Hammett substituent constants of polysubstituted compounds, so that top reducing candidates can be determined and further evaluated at the DFT level while minimizing computational expense. Data set tests showed only training with 30 molecules, out of a total of 150 compounds in the set produced highly accurate frontier orbital energies,
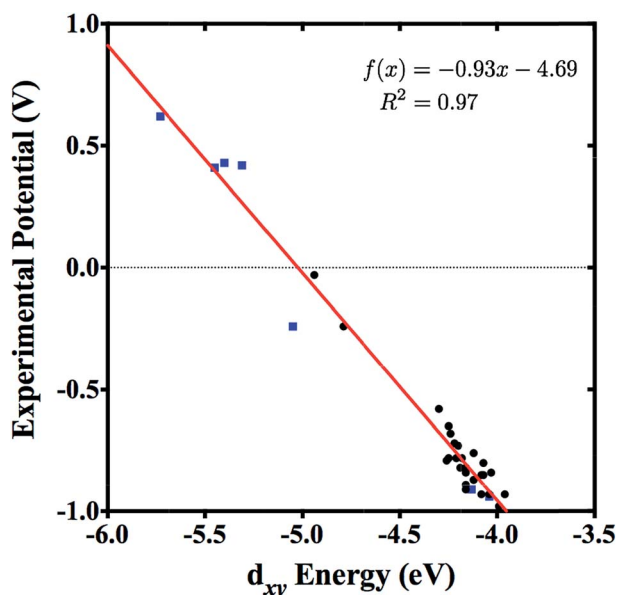

Fig. 2 Experimental potentials of 32 $W(\equiv CR')L_4X$ complexes plotted against their corresponding DFT (B3LYP) d_{xy} energies, with basis set LANL2DZ used for W, Cl, Br, and I atoms, and basis set 6-311G* used for all other atoms. A structural benchmarking study by Rudshteyn *et al.* showed that this chosen level of theory was in agreement with experiment.[6] Data was taken from ref. 6 including only reversible (black circles) and quasi-reversible (blue squares) experimental potentials.

$$f(x) = -0.93x - 4.69$$
$$R^2 = 0.97$$

demonstrating the ability to produce accurate predictions from a modest number of calculations.

Methods

Computational modeling

The series of compounds W($\equiv$CArR)L$_4$X includes 5 substituent options for the R position, 6 for L and 5 for X (Fig. 1). Note that in this study R denotes the ligand on the aryl group as shown in Fig. 1 and is not R′ which includes the aryl group and the organic substituent, as in the previous paper.[6] The ligands are commercially available or easily accessible, and are also synthetically viable options for the tungsten catalyst of interest. For the purpose of redox potential calculations, solvation energies were calculated using single point calculations under the SMD dielectric continuum model[39] for the solvent THF ($\varepsilon = 7.43$),[35] the most popular solvent used in studies of these tungsten–benzylidene complexes.[4] The orbitals with symmetry d$_{xy}$ (typically the HOMO) and π^* (typically the LUMO) were identified by visual inspection of DFT-optimized molecules, using Avogadro 1.2.0.[32,40] Visual examples of these orbitals are displayed in the ESI.† The d$_{xy}$ energies and d$_{xy}$–π^* energy gaps were tabulated and analyzed as shown in Fig. 5.

Redox potentials ($E_{1/2}$) were computed using the Born–Haber cycle at the DFT level of theory (B3LYP[36]/Def2SVP[37,38]), relative to the computed potential for the complex W(CPh)(dmpe)$_2$Cl. The Def2SVP basis set is worse than the basis set used for this catalyst in the previous paper,[6] but is cheaper for calculations and is shown to perform comparably to experimental values, like its predecessor, through the scaling procedure detailed below. The expression for $E_{1/2}$ is given, as follows:

$$E_{1/2} = \frac{\Delta G_{ox,solv}}{nF} = \frac{\Delta G_{solv}(III) - \Delta G_{solv}(II)}{nF} \quad (2)$$

where n is the number of moles of electrons in the redox reaction ($n = 1$ in this study) per mole of oxidized complex, F is Faraday's constant, and $\Delta G_{solv}(II)$ and $\Delta G_{solv}(III)$ are the free energies of solvation (with thermal corrections) of the d^2 tungsten complexes and oxidized d^1 complexes, respectively. The redox potential of complex W(CPh)(dmpe)$_2$Cl was experimentally determined and chosen as an internal reference.[6] The calculated redox potential for that complex was scaled to its experimental value (-0.82 V vs. FeCp$_2^{0/+}$). The redox potential of another complex, W(CH)(dmpe)$_2$Cl, was also calculated (-0.80 V) and compared to its corresponding experimental value (-0.84 V) to gauge and verify upon the effectiveness of the reference.

The previous study on this tungsten catalyst determined that dispersion corrections were only necessary for one of their potential catalysts.[6] To show that these corrections are not necessary for our molecules, a selected ten of our 150 molecules were re-optimized using dispersion-corrected DFT (ωB97XD[41]/Def2SVP), with their resulting energies shown in the ESI.† It was found that the absolute energies of the d$_{xy}$ orbital and the d$_{xy}$–π^* gap are systematically altered, making their relative energies approximately the same as their non-dispersion-corrected energies. Therefore, we conclude that our machine learning

models would capture the same trends regardless of the use of dispersion-corrected functionals, thereby rendering dispersion calculations of all of our candidates superfluous.

Data sets

For most of the data sets used, each compound was defined by 11 parameters, consisting of an output label corresponding to the energy of the frontier orbital with d$_{xy}$ symmetry or energy gap d$_{xy}$–π^* and 10 input Hammett parameters associated with the substituent groups, including R, X, and 3 L ligands described by σ_m and σ_p. The fourth ligand L was determined by the other three choices of L since we imposed a symmetry constraint that should facilitate synthesis and assembly (Fig. 1). Note, ethyl groups were used in place of the alkyl chains of equatorial bidentate ligands, as shown in Table 1 (e.g., tmeda becomes two NEt$_2$) since ethyl groups mimic the alkyl chains of the original ligands and the Hammett parameters of the bidentate ligands are not available. For the purposes of comparison, one data set used atomic coordinates instead of Hammett parameters as its input. In atomic coordinate input, the corresponding period and valence electron number of each connecting atom of a substituted ligand acted as input parameters. For example, substituting a methyl would give input parameters of 2 and 4 for that ligand. This led to a total of 10 input parameters for the 5 substitution positions. Regardless of parameterization, all molecules are labeled using the code RLX where R, L, and X are the corresponding codes for the ligands, as shown in Table 1 and Fig. 1. For example, complex **352** corresponds to OMe in the R position, cis-dmnpe for the L ligands, and Cl at the X site.

From these two parameterizations, ten data sets of 150 molecules each were formed and are shown in Fig. 3. Data sets **1A** and **1B** use a random 120 : 30 train : test split, are described by the atomic coordinate input parameters, and use d$_{xy}$ energy (**1A**) or d$_{xy}$–π^* energy gap (**1B**) as the output parameters. Data sets **2A** and **2B** use a random 120 : 30 train : test split, are described by the ten Hammett parameters input, and use d$_{xy}$ energy (**2A**) or d$_{xy}$–π^* energy gap (**2B**) as the output parameters. Data sets **3A** and **3B** use a fixed 30 : 120 train : test split, are described by the ten Hammett parameters input, and use d$_{xy}$ energy (**3A**) or d$_{xy}$–π^* energy gap (**3B**) as the output parameters. The 30 molecules used for training in the **3A**/**3B** data sets were hand-chosen to cover the feature space as much as possible with

Table 1 Molecules are named using numbers corresponding to the ligands at the R, L, and X sites, as shown below. For example, molecule **224** has Me in the R position, dmpe modeled as PEt$_2$ in the L position, and SMe in the X position

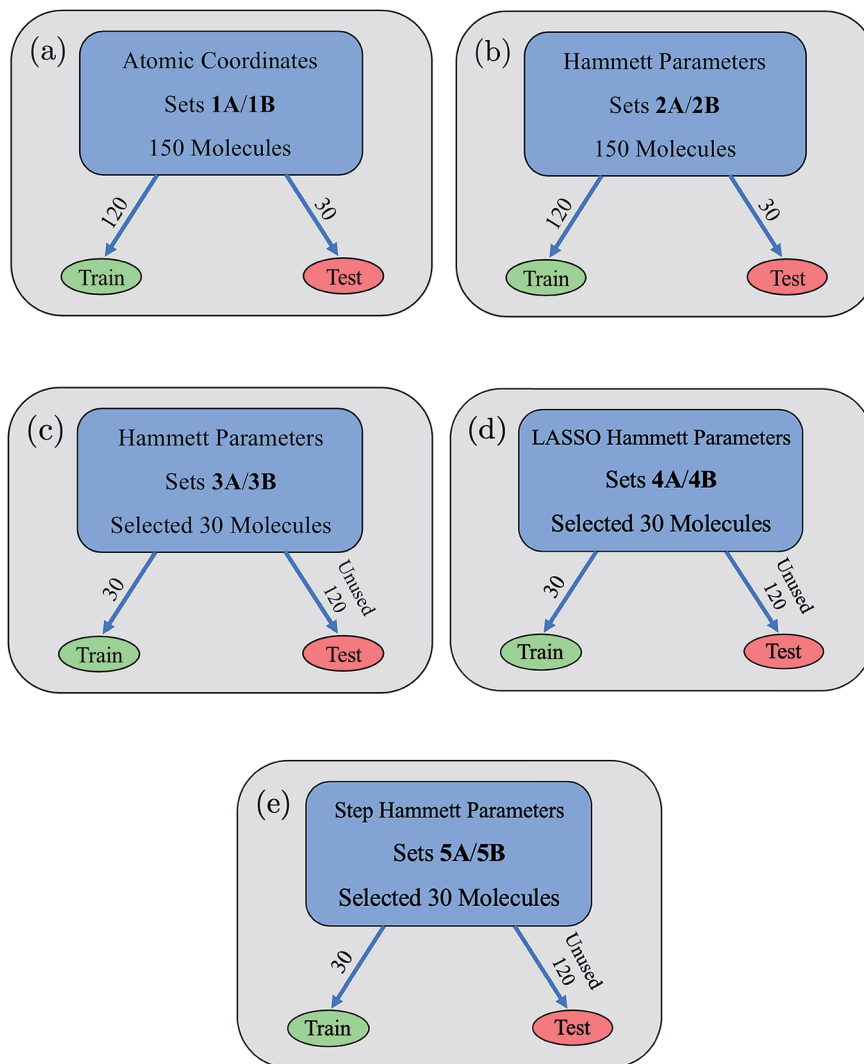|	R	L$_1$	L$_2$	L$_3$	X
1	H	NEt$_2$	NEt$_2$	NEt$_2$	F
2	Me	PEt$_2$	PEt$_2$	PEt$_2$	Cl
3	OMe	AsEt$_2$	AsEt$_2$	AsEt$_2$	OMe
4	SMe	SEt	SEt	SEt	SMe
5	NMe$_2$	NEt$_2$	PEt$_2$	PEt$_2$	NMe$_2$
6		NEt$_2$	PEt$_2$	NEt$_2$	

Fig. 3 (a–e) The ten main data sets used in our neural network and their training/testing splits are shown. "A" and "B" refer to data sets with the label d$_{xy}$ energy and d$_{xy}$–π* energy gap, respectively. Data sets **1A/1B**, **2A/2B**, **3A/3B** each have ten input Hammett parameters, while sets **4A/4B** and **5A/5B** have less than ten input Hammett parameters due to the use of feature selection methods to create them.

equal representation amongst the various ligand options at each site. Sets **4A/4B** and **5A/5B** were formed *via* multivariate linear regression models performed on sets **3A/3B** and will be further discussed in a later section. All data sets are provided in the ESI.†

Principal component analysis (PCA)

PCA was performed with RStudio 1.1.442,[42] using the 'factoextra' library,[43] for data sets **2A/2B** to determine what correlations existed between the Hammett parameters and the labels used in the regressive methods. The resulting rotation matrix was used to determine which parameters covered the most variance in the output data, providing an effective way of predicting whether the regressive methods could derive a correlation pattern. The amount of correlation between input and labels provided insights into how much data was needed for each degree of freedom, leading to the construction of data sets **3A/3B**.

Neural network

A neural network was coded in python using the Sequential model in the Keras library,[44] with a Tensorflow backend. The network, shown in Fig. 4, included two hidden layers with 12 and 8 neurons along with the input and output layers of size 10 and 1, respectively. For compilation of the model, the mean-squared error (MSE) was used as the loss function while the 'Adam' algorithm[45] with default parameters was used as the optimizer. A loss or cost function is a function used to tell how far the predicted results are from the actual results. This cost is then used with the Adam algorithm, which is a gradient based algorithm capable of dealing with noisy data, to determine how the weights are updated after every round of training. The hyperparameters, number of layers, nodes per layer, and activation functions employed were chosen because they produced optimal results. A trial and error procedure where hyperparameters, activation functions, and layer construction were
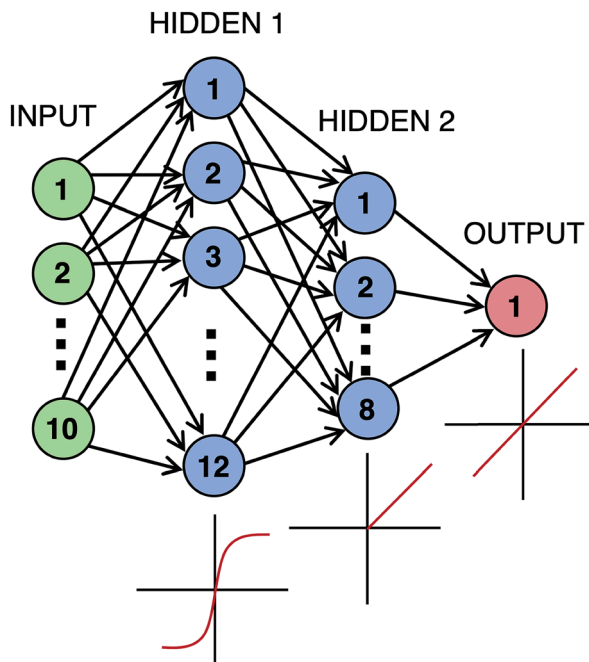
Fig. 4 Diagram of the implemented artificial neural network. The first hidden layer employs a tanh activation function, the second layer a rectified linear unit (ReLU) activation function, and the output a linear activation function.

adjusted one at a time until no improvement was observed was used to determine this optimality. A plausible explanation for why the hyperbolic tangent function works as a good first activation function could be because the domain of the Hammett substituent constants is centered around 0 and is mostly between -1 and 1.[2] In addition, the PCA results below show both uncoupled and coupled ligand interactions contributing to the output parameters. With such complex interactions, the inclusions of a nonlinear function like hyperbolic tangent, a linear function, and *ReLU*, which is partially linear, offer the ability to describe these relationships. The optimization of network parameters during training of each data set required 220 epochs to reach convergence, with a batch size of 2. Convergence was defined as the number of epochs at which a minimum MSE occurred without overfitting. K-fold cross-validation was performed with a 90% training, 10% validation breakdown.

The MSE of predicted energies relative to the DFT values was recorded for each round of 220 epochs for both training and testing data. The testing MSE values were averaged over 90 rounds for data sets **2A**/**2B** and 30 for **1A**/**1B** and **3A**/**3B**. A standard deviation was calculated for each average MSE. The molecules chosen for the 120 : 30 training : testing split for **1A**/**1B** and **2A**/**2B** are random for each round. For the data sets **3A**/**3B**, the network evaluated the MSE based on the 120 unused molecules in the test set, which were the same for all rounds because the training set was pre-selected. The networks parametrized with **3A**/**3B** were then used to predict the labels of all 150 molecules (including the 30 complexes used for training), which were then compared to their corresponding

DFT values. Performing this test demonstrated the capabilities and limitations of the resulting networks as applied to predicting the full energy spectrum of frontier orbitals. Welch two sample *t*-tests were performed to see whether the models generalized well, comparing the average MSE of the predicted energies between the 30 molecules in **3A**/**3B** and the remaining 120 not included in those sets. A significance level $p = 0.05$ was used to determine whether the means of the MSE of the two subsets deviated significantly from one another. If the average MSE of the 30 training molecules is statistically less significant than that of the other 120, then the model did not generalize well to the test candidates and may have been overfitted to the training data.

Alternative regressive models

Multivariate Linear, LASSO, Ridge, and Gaussian Process regressions were all implemented using the Scikit Learn package.[46] The cost functions for each of the linear regressions can be seen below where x_{ij} are inputs, y_i are the expected value, and w_j are the weights. The Gaussian process regression used Algorithm 2.1 from Rasmussen and Williams with a radial basis function kernel (covariance).[47]

$$\text{Linear regression cost} = \sum_{i=1}^{N}\left(y_i - \sum_{j=0}^{M} w_j x_{ij}\right)^2 \tag{3}$$

$$\text{Ridge regression cost} = \sum_{i=1}^{N}\left(y_i - \sum_{j=0}^{M} w_j x_{ij}\right)^2 + \alpha \sum_{j=0}^{M} w_j^2 \tag{4}$$

$$\text{LASSO regression cost} = \sum_{i=1}^{N}\left(y_i - \sum_{j=0}^{M} w_j x_{ij}\right)^2 + \alpha \sum_{j=0}^{M} |w_j| \tag{5}$$

The parameter α in Ridge and LASSO was tested with the values 0, 0.001, 0.005, and 0.01. LASSO and Ridge methods were tested with and without cross validation. Cross-validation is a method used to prevent overfitting and improve a model's generalization by allocating a subset of data as validation data during each round of training that will be used as a test set to generate the cost. This cost is used to update the weights of the regressive method. Without cross-validation, this cost is determined by the training data. However, using the same training data every round may cause overfitting because the weights are being tuned precisely to the same data. Instead, if cross-validation is performed, the weights will be less biased towards the training data and will give a better estimate of the accuracy of the model on unseen data. Each method was tested using data sets **3A**/**3B** as these data sets offered the most promise for utility and accuracy. The LASSO method has a built-in feature selection that was used on set **3A** using $\alpha = 0.01$ to select parameters for new data sets **4A**/**4B**, which use d_{xy} energy (**4A**) or d_{xy}–π^* energy gap (**4B**) as the output parameters. Similar to what was done with sets **3A**/**3B**, these new data sets were trained on the neural network and tested on the energies of the 120 unused molecules. All of the previously mentioned

regressive methods, including the neural network, were also tested with data sets **4A/4B** in order to determine the effects of the LASSO feature selection.

Using stepwise regression, we found another set of alternative models that predicted the d_{xy} energy and $d_{xy}–\pi^*$ energy gap well. Forward selection, backward elimination, and bidirectional elimination stepwise regression were used with selection criterion of either Akaike information criterion (AIC)[48] or Bayesian information criterion (BIC),[49] giving a total of six regressions for each label. Formulas for AIC and BIC are displayed in eqn (6) and (7),

$$AIC = -2 \log L + 2p \tag{6}$$

$$BIC = -2 \log L + \log(n)p \tag{7}$$

where L is the likelihood function of a given model, p is the number of parameters, and n is the number of observations. The two selection criteria are both estimators of relative qualities of statistical models, and are used to maximize the goodness of fit of the model while keeping the model simple by penalizing for the number of parameters p, thereby discouraging overfitting. These regressions were performed using the 'step' function in RStudio 1.1.442 (ref. 42) on training sets **3A/3B** for a total of 12 different regressions. The suggested Hammett parameters from these regression models were then used to convert **3A/3B** to data sets **5A/5B**, and these new data sets were trained on the neural network and tested on the energies of the 120 unused molecules, likewise to what was done for **3A/3B**.

The MSE's for these multivariate regression models were calculated differently than those for the neural network comparison of data sets **1A/1B**, **2A/2B**, and **3A/3B** (Table 3). For the MSE's seen in Table 4, the training sets **3A/3B**, **4A/4B**, and **5A/5B** were used to predict the energies of the unused 120 molecules for those data sets following each round (220 epochs) of training. These test energies were averaged over 30 rounds of training, and then the MSE of those average energies was calculated. The reason why we calculated the MSE's differently for the neural networks in Table 3 was to show the standard deviation of the MSE's between our training rounds for the neural network. In contexts where there are restrictions on averaging over training rounds, it is important to know that the MSE for a given round of training does not deviate too significantly from its average. Moreover, Welch two sample t-tests identical to those used for the neural networks were performed on the training and testing MSE of all regression models on data sets **3A/3B** to determine generalizability.

Results and discussion

DFT calculations

The DFT d_{xy} energies and $d_{xy}–\pi^*$ energy gaps of all 150 molecules in the sets (provided in the ESI†) were obtained after full geometry optimization. Consistent with changes in the coordination sphere of tungsten, we find that the d_{xy} energies and $d_{xy}–\pi^*$ energy gaps are most sensitive to changes in the L ligands. When nitrogen is in the L ligand (L = tmeda, *cis*-dmnpe, *trans*-

dmnpe), the catalysts have much higher d_{xy} energies than the other compounds. The axial ligands have a less significant effect on the d_{xy} energy, consistent with the π^* orbital being oriented along the z-axis of the molecule. The $d_{xy}–\pi^*$ gaps remain in the UV-visible range (<4 eV) for all complexes, keeping the photoexcitation energies suitable for solar photocatalytic applications.

Principal component analysis

PCA of data sets **2A/2B** gave three major components, with percentages reported in Table 2 (rotation matrices provided in the ESI†). Each of the top three principal components corresponds to high correlation between one of the three varied substitutional sites and the output label. The rotation matrix of our analyses reveals that the equatorial ligands are responsible for the most significant variance in both data sets, consistent with earlier studies.[4] The Hammett parameters in the L positions show anticorrelation with the d_{xy} energy (therefore a positive correlation with the $d_{xy}–\pi^*$ gap), which can be observed in the biplot shown in the ESI.† These results are consistent with the fact that substituents with more negative Hammett substituent constants are better electron-donors as usually observed in electron density trends. The second and third principal components, which mostly correspond to the X and R sites, do not correlate strongly with either label although they are responsible for about 15–18% of the variance. From the rotation matrices, the large isolation of each substitution site into the three highest variance principal components indicates, as expected, that the largest contributions to the energies are the uncoupled ligands which may be expected to give a linear relationship. Subsequent components which make up a total of 18.4% and 19.2% respectively of the variance in the d_{xy} and $d_{xy}–\pi^*$ gap are coupled ligand contributions that involve mixtures the of the R, L, and X substitution sites. These coupled mixtures may be non-linear in nature. Based on the R, L, and X components each being responsible for high amounts of variance, all features were kept for the **2A/2B** data sets.

Neural network

Table 3 shows the average MSE for each of the neural network data sets. These results show that the neural networks based on Hammett parameters perform better than those based on atomic coordinates and thereby better predict the d_{xy} energies and $d_{xy}–\pi^*$ energy gaps. With an MSE below 0.004, the **2A/2B** model is in semiquantitative agreement with DFT. However,

Table 2 Percentage contributions to the variance from the first three principal components of data sets **2A** and **2B**. PC1 has correlation between the label and the L parameters, while PC2 and PC3 correlate with the X and R parameters, respectively

Label	PC1	PC2	PC3
$E(d_{xy})$	48.3%	17.9%	15.4%
$E(\pi^*)–E(d_{xy})$	47.2%	17.9%	15.7%

Table 3 Mean-squared error in eV^2, averaged over 30 runs, of randomly chosen test sets of 30 molecules for **1A/1B** and **2A/2B** and a selected test set of 120 molecules for **3A/3B**

Data sets	$E(d_{xy})$ MSE	$E(\pi^*)–E(d_{xy})$ MSE
1A/1B	0.0088(51)	0.0106(28)
2A/2B	0.0036(14)	0.0035(13)
3A/3B	0.0107(29)	0.0068(15)

that level of accuracy results from a large data set including 80% of all possible molecules.

Table 3 reports the average MSE for the sets **3A** and **3B**, highlighting the accuracy of the neural networks generated with a minimum amount of training. Note that **3A** and **3B** predicted both labels well, with an average MSE of 0.0107 for the d_{xy} energy and 0.0068 for the $d_{xy}–\pi^*$ gap, employing only a quarter

Fig. 5 Correlation between the NN-predicted and DFT-obtained energies for the d_{xy} orbitals (a) and $d_{xy}–\pi^*$ gaps (b) of molecules in data sets **3A/3B**.

of the amount of training data used by the full sets. Fig. 5a and b show the correlation plots for all 150 predicted values from the sets **3A/3B** of energies d_{xy} and $d_{xy}–\pi^*$ gap, respectively, *versus* their corresponding DFT values. The slope and correlation coefficient near 1 highlight the level of correlation and prediction accuracy for both labels. We note that the **1A** and **1B** sets have the same level of performance as **3A** and **3B** but require 4 times more data (120 DFT calculations) for parameterization. Furthermore, there is evident clustering of data points in Fig. 5a; this clustering can be explained by the small amount of training data, as when **2A** is trained and used to predict all 150 energies, the clustering disappears, which is shown in the ESI.†

Molecule **515** is identified by the neural network (NN) for set **3A** to be optimal as a reducing agent. According to DFT, however, **515** has the second-highest d_{xy} energy with a reduction potential of −2.40 V *vs.* $FeCp_2^{0/+}$, only 50 mV below that of **513** which is the most reducing catalyst. Nevertheless, **513** is predicted by the NN to be within the top 5% – *i.e.*, within a standard deviation of the d_{xy} energy of **515**. Other complexes, such as **511**, **313** and **315** with tmeda ligands also exhibit great reducing power. This is expected, as the stronger π-donating ability of tmeda compared to that of the other equatorial options raises the d_{xy} orbital energy more and decreases stabilization due to π-backbonding. The predicted rankings are even more accurate for the $d_{xy}–\pi^*$ gaps in set **3B**. The two molecules with the largest $d_{xy}–\pi^*$ gaps (**521**, **541**) are identical for both the NN and DFT predictions, as well as the four molecules with the smallest gaps (**114**, **214**, **414**, **115**). This is again consistent with the π-accepting trends in the equatorial plane, as the more π-accepting ligands have higher $d_{xy}–\pi^*$ energy gaps because of the lowering of the d_{xy} orbital energy due to stronger π-backbonding. Furthermore, the NN predicts that all $d_{xy}–\pi^*$ gaps are within the UV-visible energy range, consistent with DFT. The parity plots formed from training sets **2A/2B** containing predictions of all 150 energies, displayed in the ESI,† show a small set of outliers that all contain sulfur in the equatorial plane. Further exploration is needed to examine why the neural network fails to predict the energies of those molecules well.

Fig. 6 shows complex **513**, which is the most promising photo-reducing complex since it has the highest d_{xy} energy and a $d_{xy}–\pi^*$ energy gap within the visible range.

These results suggest that the predicted potential for **513** of −2.45 V should be close to the actual experimental value since we have previously gauged the accuracy of our potentials to be in good agreement with the experimentally determined values.[4] We have also performed a two-way *t*-test to compare the MSE's between the molecules used for training and the molecules used for testing for sets **3A** and **3B**. The *p*-values of the *t*-tests for **3A** and **3B** were both 0.52, well above the significance threshold of 0.05. Consequently, it is natural to conclude that our training from the **3A/3B** has generalized well, as the mean contributions in MSE between the 30 training candidates and 120 test candidates are not significantly different. Furthermore, we have checked that our model did not overfit the data, as shown in the ESI† by the graph of the training and validation loss for d_{xy} energies of all 150 molecules. These results underscore the
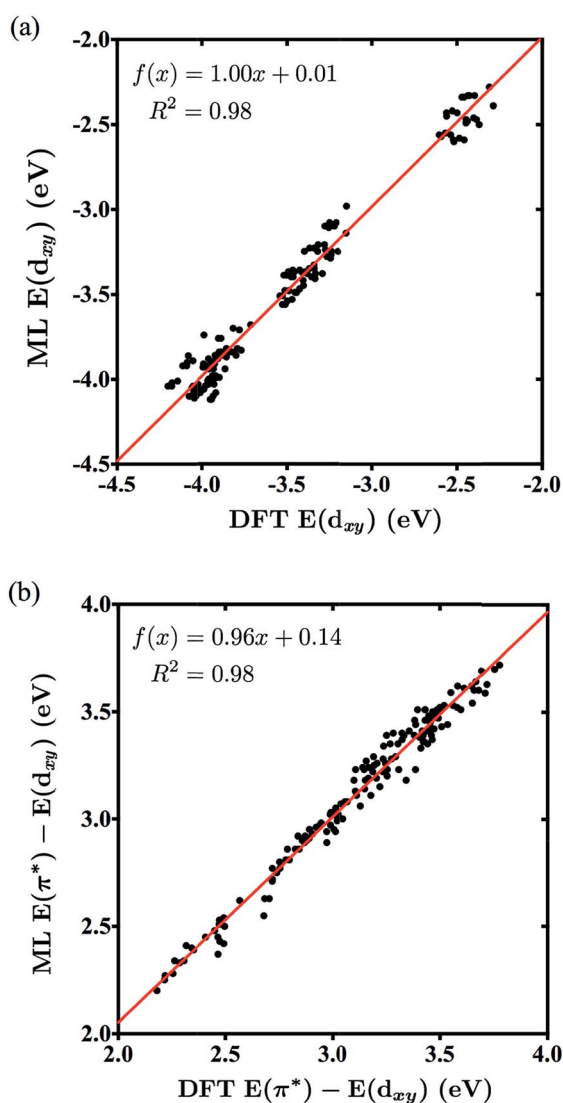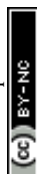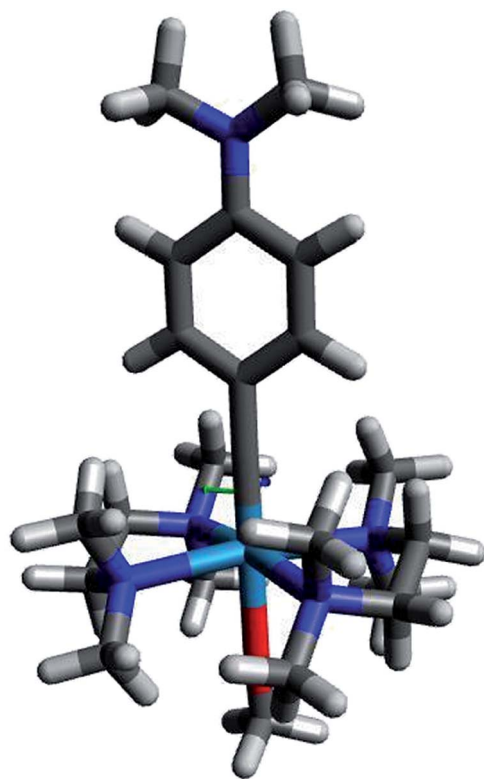
Fig. 6 Compound **513**, predicted to be highly reductive, with a redox potential of −2.45 V *vs.* FeCp$_2$$^{0/+}$. Color code: gray = C; white = H; dark blue = N; red = O; light blue = W.

computational power of the NN methodology, since the expense of training and testing is negligible compared to that of DFT calculations.

Alternative regressive models

The MSE results from the alternative regressive models and the neural network for data sets **3A/3B** and **4A/4B** are shown in

Table 4 Mean squared error values from trials with linear, LASSO (with and without CV), ridge (with and without CV), and stepwise regressions, and from trials of the neural network model are shown for data sets **3A/3B** and **4A/4B** and **5A/5B**. Note that some values are from identical regressions, such as the linear regression of **5A** being identical to the stepwise regression of **3A**

	5A	4A	3A	5B	4B	3B
Linear	0.0026^a	0.0026	0.0026	0.0061^a	0.013	0.0059
Ridge ($\alpha = 0.01$)	—	0.0026	0.0026	—	0.013	0.0060
LASSO ($\alpha = 0.01$)	—	0.0092^a	0.0092^a	—	0.020^a	0.020^a
NN (with CV)	0.0056	0.0038	0.0081^b	0.0034	0.013	0.0034^b
Ridge CV	—	0.0033	0.0028	—	0.014	0.0088
LASSO CV	—	0.0032	0.0026	—	0.016	0.0079
Stepwise	—	—	0.0026^a	—	—	0.0061^a
Gaussian process	—	0.013	0.0079	—	0.060	0.0082

^{a} These models have identical models with the same MSE's. ^{b} The NN MSE's for **3A** and **3B** shown here are calculated differently than those for Table 3, as explained in the Methods.

Table 4. LASSO regression on set **3A** generated **4A/4B**, which have parameters R σ_m, R σ_p, L$_1$ σ_p, L$_2$ σ_m, L$_2$ σ_p, L$_3$ σ_p, and X σ_p as the input. As seen in Table 4, the best predictive models, as determined by lowest MSE, are linear and ridge regression for the d$_{xy}$ energy, and the neural network for the d$_{xy}$–π* energy gap. While those are the best results purely by the absolute MSE's, it is important to note that the MSE's for every model in each column of Table 4 are very close with the exception of LASSO without cross validation. Without cross validation, LASSO is susceptible to completely removing important features as it did for the d$_{xy}$–π* energy gap where the features selected were only R σ_p, L$_1$ σ_p, L$_2$ σ_p, L$_3$ σ_p. Note there is no longer a feature describing the X position ligand, which was shown by PCA to contain about 15% of the variance in both outputs. It is likely for this reason that the LASSO model had an MSE much higher than those of the other models using the **3B** data set. Comparing the use of LASSO parameters between the **4A/3A** data sets, it can be seen that the use of LASSO parameters improves the NN case. We note that the extra regularization does not improve the linear, ridge, or LASSO regressions. In fact, the use of the LASSO parameters worsens the cross validated LASSO and ridge cases. Using the LASSO parameters, which were derived from the d$_{xy}$ output, also increases the MSE for the d$_{xy}$–π* cases. Combining the above results and the LASSO data set's failure to consistently produce better MSE's than other data sets, we conclude that further examination of the **4A/4B** data sets is unnecessary. All LASSO and ridge regressions on the **3A/3B** data sets, both with and without cross validation, are found to generalize well between training and testing data as seen in Table 5.

The six step regressions used for each label agreed on one particular model for the d$_{xy}$ energy and another one for the d$_{xy}$–π* energy gap. For the d$_{xy}$ energy, the regression model suggested R σ_p, L$_1$ σ_m, L$_1$ σ_p, L$_2$ σ_m, L$_3$ σ_m, and X σ_p as the Hammett parameters; for the d$_{xy}$–π* energy gap, the regression model suggested R σ_m, R σ_p, L$_1$ σ_p, L$_2$ σ_m, L$_2$ σ_p, X σ_m, and X σ_p. The linear regressions for the d$_{xy}$ energy and d$_{xy}$–π* energy gap models gave MSE of 0.0026 and 0.0061 eV^2, respectively, as shown in Table 4. We see in Table 5 that while the **5A** data set's training generalizes well, the **5B** data set's training does not.

Table 5 Welch two-sample *t*-tests were performed on the training and test MSE's of each regression. The corresponding *p*-values are displayed below. A significance threshold of $p = 0.05$ was used to determine whether the training and test contributions to the MSE's were statistically significantly different

	d$_{xy}$ *t*-test	d$_{xy}$–π* *t*-test
Linear	0.96	0.56
Ridge ($\alpha = 0.01$)	0.96	0.50
LASSO ($\alpha = 0.01$)	0.88	0.99
NN (with CV)	0.53	0.53
Ridge CV	0.96	0.56
LASSO CV	0.98	0.48
Stepwise	0.99	0.0009
Gaussian process	8.7×10^{-6}	1.1×10^{-9}

This could be easily explained by the step regression removing all parameters describing the L_3 ligand for the $d_{xy}-\pi^*$ energy gap model, which would introduce error in the prediction of the catalyst's frontier orbital energies when generalized to the unused 120 molecules.

In a comparison of ridge regression cases with and without cross validation, a predictable increase of MSE is seen when including cross validation. As ridge regression turned into linear regression when the hyperparameter α went towards zero (shown in the ESI†), it can be extrapolated that the same pattern of increased error would be seen between cross validated linear regression and normal linear regression. The increased error with cross validation is predictable because the model is made less dependent on individually picked training data, making it more generalizable which tends to make individual data points less well described. As a generalizable model is desired, this hit to accuracy is generally an acceptable tradeoff. However, since ridge regression only outperforms the NN in the d_{xy} case and the NN does include cross validation, neither model can be considered distinctly better.

Comparing MSE's for our models using **3A**, the neural network performed worse than the linear, ridge, and step regressions, while for **3B**, the neural network had the lowest MSE. Similar results are found for sets **4A/4B** and **5A/5B**, as for both sets it is observed that the linear model outperforms the NN for the d_{xy} energy but not for the $d_{xy}-\pi^*$ energy gap. This suggests that there likely is more non-linear contribution from the Hammett parameters to the $d_{xy}-\pi^*$ energy gap than to the d_{xy} energy. Further exploration is needed to analyze the source behind these non-linear contributions.

It is seen that the linear, ridge, ridge cross-validated, and LASSO cross-validated regressions developed patterns of prediction similar to those of the neural network. For these regressions, once again the actual top reducing agent was found within the top 5% based off of d_{xy} energies, and the actual second-best reducing agent was predicted to be the best. Furthermore, the largest DFT $d_{xy}-\pi^*$ energy gap was correctly predicted by these models, and the second biggest was within the top 5%. As expected, the lack of generalization for the LASSO without cross-validation case is less accurate, finding the DFT second largest $d_{xy}-\pi^*$ energy gap only in the top 10%. Gaussian process regression also had difficulty, only predicting the top reducing agents in the top 10%, and predicting the largest gap in the top 5% and the 2nd largest gap to be the biggest.

Hammett substituent constants of varied ligands, the methodologies were able to predict the reducing power of tungsten complexes by accurately identifying the candidates with the highest d_{xy} energies. The linear, ridge, ridge cross-validated, LASSO cross-validated, and NN methods were thus able to capture the electron-withdrawing/donating trends of multiple substituents, aryl or not, showing that the resulting models efficiently harness the breadth of existing Hammett parameters in a new manner. The second-highest reducing catalyst, as predicted by the DFT d_{xy} energy, was found to be the optimal candidate according to these models, while the highest was found within the top 5%. These models produced results that were even better for predictions of $d_{xy}-\pi^*$ energy gaps, since the molecules with the largest and smallest gaps were predicted correctly. While the NN performed better for the $d_{xy}-\pi^*$ energy gap than the alternative methods, the alternative methods proved to be better models for the d_{xy} energy, suggesting that these alternative multivariate linear models should always be evaluated in addition to the NN for this methodology, with a keen focus on generalizability. The optimal catalyst has tetramethylethylenediamine (tmeda) equatorial ligands and axial OMe, with an oxidation potential of -2.45 V. It also satisfies the constraint of $d_{xy}-\pi^*$ energy differences in the visible range, making it a promising candidate for a wide range of reactions, including reduction of CO_2.

The introduced Hammett NN and alternative regressive machine learning models have been demonstrated as applied to the prediction of energies of frontier orbitals and could be generalized for a wide range of other molecular properties simply by training the models with calculations of the desired properties with DFT. Because the Hammett parameters are tabulated for hundreds of substituents, the Hammett NN could address a broad class of molecules simultaneously varying multiple sites.

Conflicts of interest

There are no conflicts to declare.

Acknowledgements

Conclusions

We have introduced the use of substituent Hammett parameters as features in regressive machine learning models and have applied the tested models to predict energies of frontier orbitals of highly reducing tungsten–benzylidyne complexes W($\equiv$CArR)L_4X with varied R, L, and X ligands. We have shown that these models can accurately predict frontier orbital energies, requiring only a modest computational training cost, thus bypassing the significant cost of high-throughput screening based on DFT. Using a constant molecular framework and the

References

1 L. P. Hammett, The Effect of Structure upon the Reactions of Organic Compounds. Benzene Derivatives, *J. Am. Chem. Soc.*, 1937, **59**(1), 96–103.

2 C. Hansch, A. Leo and R. W. Taft, A survey of Hammett substituent constants and resonance and field parameters, *Chem. Rev.*, 1991, **91**(2), 165–195.

3 H. H. Jaffé, A Reëxamination of the Hammett Equation, *Chem. Rev.*, 1953, **53**(2), 191–261.

4 D. E. Haines, D. C. O'Hanlon, J. Manna, M. K. Jones, S. E. Shaner, J. Sun and M. D. Hopkins, Oxidation-Potential Tuning of Tungsten–Alkylidyne Complexes over a 2 V Range, *Inorg. Chem.*, 2013, **52**(16), 9650–9658.

5 B. M. Lovaasen, J. V. Lockard, B. W. Cohen, S. Yang, X. Zhang, C. K. Simpson, L. X. Chen and M. D. Hopkins, Ground-State and Excited-State Structures of Tungsten–Benzylidyne Complexes, *Inorg. Chem.*, 2012, **51**(10), 5660–5670.

6 B. Rudshteyn, H. B. Vibbert, R. May, E. Wasserman, I. Warnke, M. D. Hopkins and V. S. Batista, Thermodynamic and Structural Factors that Influence the Redox Potentials of Tungsten–Alkylidyne Complexes, *ACS Catal.*, 2017, **7**(9), 6134–6143.

7 R. E. Da Re and M. D. Hopkins, Electronic spectroscopy and photophysics of metal–alkylidyne complexes, *Coord. Chem. Rev.*, 2005, **249**(13), 1396–1409.

8 W. L. Jorgensen, The many roles of computation in drug discovery, *Science*, 2004, **303**(5665), 1813–1818.

9 D. Xiao, L. A. Martini, R. C. Snoeberger, R. H. Crabtree and V. S. Batista, Inverse Design and Synthesis of acac-Coumarin Anchors for Robust TiO_2 Sensitization, *J. Am. Chem. Soc.*, 2011, **133**(23), 9014–9022.

10 R. M. Balabin and E. I. Lomakina, Neural network approach to quantum-chemistry data: Accurate prediction of density functional theory energies, *J. Chem. Phys.*, 2009, **131**(7), 074104.

11 V. P. Solov'ev, Y. A. Ustynyuk, N. I. Zhokhova and K. V. Karpov, Predictive Models for HOMO and LUMO Energies of N-Donor Heterocycles as Ligands for Lanthanides Separation, *Mol. Inf.*, 2018, **37**, 1800025.

12 X. Wang, L. Wong, L. Hu, C. Chan, Z. Su and G. Chen, Improving the Accuracy of Density-Functional Theory Calculation: The Statistical Correction Approach, *J. Phys. Chem. A*, 2004, **108**(40), 8514–8525.

13 M. Rupp, A. Tkatchenko, K.-R. Müller and O. A. von Lilienfeld, Fast and Accurate Modeling of Molecular Atomization Energies with Machine Learning, *Phys. Rev. Lett.*, 2012, **108**(5), 058301.

14 F. Pereira, K. Xiao, D. A. R. S. Latino, C. Wu, Q. Zhang and J. Aires-de-Sousa, Machine Learning Methods to Predict Density Functional Theory B3LYP Energies of HOMO and LUMO Orbitals, *J. Chem. Inf. Model.*, 2017, **57**(1), 11–21.

15 G. Montavon, M. Rupp, V. Gobre, A. Vazquez-Mayagoitia, K. Hansen, A. Tkatchenko, K.-R. Müller and O. A. Von Lilienfeld, Machine learning of molecular electronic properties in chemical compound space, *New J. Phys.*, 2013, **15**(9), 095003.

16 K. Hansen, G. Montavon, F. Biegler, S. Fazli, M. Rupp, M. Scheffler, O. A. Von Lilienfeld, A. Tkatchenko and K.-R. Müller, Assessment and validation of machine learning methods for predicting molecular atomization energies, *J. Chem. Theory Comput.*, 2013, **9**(8), 3404–3419.

17 C. B. Santiago, J.-Y. Guo and M. S. Sigman, Predictive and mechanistic multivariate linear regression models for reaction development, *Chem. Sci.*, 2018, **9**(9), 2398–2412.

18 J. S. Smith, O. Isayev and A. E. Roitberg, ANI-1: an extensible neural network potential with DFT accuracy at force field computational cost, *Chem. Sci.*, 2017, **8**(4), 3192–3203.

19 Y. Li, H. Li, F. C. Pickard, B. Narayanan, F. G. Sen, M. K. Y. Chan, S. Sankaranarayanan, B. R. Brooks and B. Roux, Machine Learning Force Field Parameters from *Ab Initio* Data, *J. Chem. Theory Comput.*, 2017, **13**(9), 4492–4503.

20 F. Brockherde, L. Vogt, L. Li, M. E. Tuckerman, K. Burke and K. R. Muller, Bypassing the Kohn-Sham equations with machine learning, *Nat. Commun.*, 2017, **8**(1), 872.

21 M. Welborn, L. Cheng and T. F. Miller, Transferability in Machine Learning for Electronic Structure *via* the Molecular Orbital Basis, *J. Chem. Theory Comput.*, 2018, **14**(9), 4772–4779.

22 H. Chen, O. Engkvist, Y. Wang, M. Olivecrona and T. Blaschke, The rise of deep learning in drug discovery, *Drug Discovery Today*, 2018, **23**(6), 1241–1250.

23 Y. Liu, T. Zhao, W. Ju and S. Shi, Materials discovery and design using machine learning, *J. Materiomics*, 2017, **3**(3), 159–177.

24 J. P. Janet, L. Chan and H. J. Kulik, Accelerating Chemical Discovery with Machine Learning: Simulated Evolution of Spin Crossover Complexes with an Artificial Neural Network, *J. Phys. Chem. Lett.*, 2018, **9**(5), 1064–1071.

25 T. Lei, F. Chen, H. Liu, H. Sun, Y. Kang, D. Li, Y. Li and T. Hou, ADMET Evaluation in Drug Discovery. Part 17: Development of Quantitative and Qualitative Prediction Models for Chemical-Induced Respiratory Toxicity, *Mol. Pharm.*, 2017, **14**(7), 2407–2421.

26 J. N. Wei, D. Duvenaud and A. Aspuru-Guzik, Neural Networks for the Prediction of Organic Chemistry Reactions, *ACS Cent. Sci.*, 2016, **2**(10), 725–732.

27 J. Frey, B. F. E. Curchod, R. Scopelliti, I. Tavernelli, U. Rothlisberger, M. K. Nazeeruddin and E. Baranoff, Structure–property relationships based on Hammett constants in cyclometalated iridium(iii) complexes: their application to the design of a fluorine-free FIrPic-like emitter, *Dalton Trans.*, 2014, **43**(15), 5667–5679.

28 C. Alexiou and A. B. P. Lever, Tuning metalloporphyrin and metallophthalocyanine redox potentials using ligand electrochemical (E_L) and Hammett (σ_p) parametrization, *Coord. Chem. Rev.*, 2001, **216–217**, 45–54.

29 J. K. Hino, L. Della Ciana, W. J. Dressick and B. P. Sullivan, Substituent constant correlations as predictors of spectroscopic, electrochemical, and photophysical properties in ring-substituted 2,2′-bipyridine complexes of rhenium(i), *Inorg. Chem.*, 1992, **31**(6), 1072–1080.

30 B. H. Solis and S. Hammes-Schiffer, Substituent Effects on Cobalt Diglyoxime Catalysts for Hydrogen Evolution, *J. Am. Chem. Soc.*, 2011, **133**(47), 19036–19039.

31 K. Tanekazu and M. Hiroshi, The Effect of Substituents on the Half-Wave Potential of the Polarographic Reduction of Pyridine N-Oxide Derivatives, *Bull. Chem. Soc. Jpn.*, 1966, **39**(10), 2057–2062.

32 M. N. Ackermann, K. B. Moore, A. S. Colligan, J. A. Thomas-Wohlever and K. J. Warren, Tetracarbonylmolybdenum complexes of 2-(phenylhydrazino)pyridine ligands.:

Correlations of spectroscopic data with pyridyl substituent effects, *J. Organomet. Chem.*, 2003, **667**(1), 81–89.

33 J. E. Heffner, C. T. Wigal and O. A. Moe, Solvent dependence of the one-electron reduction of substituted benzo- and naphthoquinones, *Electroanalysis*, 1997, **9**(8), 629–632.

34 M. L. Dell'Arciprete, C. J. Cobos, J. P. Furlong, D. O. Mártire and M. C. Gonzalez, Reactions of Sulphate Radicals with Substituted Pyridines: A Structure–Reactivity Correlation Analysis, *ChemPhysChem*, 2007, **8**(17), 2498–2505.

35 M. J. Frisch, G. W. Trucks, H. B. Schlegel, G. E. Scuseria, M. A. Robb, J. R. Cheeseman, G. Scalmani, V. Barone, B. Mennucci, G. A. Petersson, H. Nakatsuji, M. Caricato, X. Li, H. P. Hratchian, A. F. Izmaylov, J. Bloino, G. Zheng, J. L. Sonnenberg, M. Hada, M. Ehara, K. Toyota, R. Fukuda, J. Hasegawa, M. Ishida, T. Nakajima, Y. Honda, O. Kitao, H. Nakai, T. Vreven, J. A. Montgomery Jr, J. E. Peralta, F. Ogliaro, M. Bearpark, J. J. Heyd, E. Brothers, K. N. Kudin, V. N. Staroverov, R. Kobayashi, J. Normand, K. Raghavachari, A. Rendell, J. C. Burant, S. S. Iyengar, J. Tomasi, M. Cossi, N. Rega, N. J. Millam, M. Klene, J. E. Knox, J. B. Cross, V. Bakken, C. Adamo, J. Jaramillo, R. Gomperts, R. E. Stratmann, O. Yazyev, A. J. Austin, R. Cammi, C. Pomelli, J. W. Ochterski, R. L. Martin, K. Morokuma, V. G. Zakrzewski, G. A. Voth, P. Salvador, J. J. Dannenberg, S. Dapprich, A. D. Daniels, Ö. Farkas, J. B. Foresman, J. V. Ortiz, J. Cioslowski, D. J. Fox, Gaussian 09, Rev. D, Gaussian, Inc., Wallingford CT, 2009.

36 A. D. Becke, Density-functional thermochemistry. III. The role of exact exchange, *J. Chem. Phys.*, 1992, **98**, 5648–5652.

37 F. Weigend and R. Ahlrichs, Balanced basis sets of split valence, triple zeta valence and quadruple zeta valence quality for H to Rn: Design and assessment of accuracy, *Phys. Chem. Chem. Phys.*, 2005, **7**(18), 3297–3305.

38 F. Weigend, Accurate Coulomb-fitting basis sets for H to Rn, *Phys. Chem. Chem. Phys.*, 2006, **8**(9), 1057–1065.

39 A. V. Marenich, C. J. Cramer and D. G. Truhlar, Universal Solvation Model Based on Solute Electron Density and on a Continuum Model of the Solvent Defined by the Bulk Dielectric Constant and Atomic Surface Tensions, *J. Phys. Chem. B*, 2009, **113**(18), 6378–6396.

40 M. D. Hanwell, D. E. Curtis, D. C. Lonie, T. Vandermeersch, E. Zurek and G. R. Hutchison, Avogadro: an advanced semantic chemical editor, visualization, and analysis platform, *J. Cheminf.*, 2012, **4**(1), 17.

41 J. D. Chai and M. Head-Gordon, Long-range corrected hybrid density functionals with damped atom-atom dispersion corrections, *Phys. Chem. Chem. Phys.*, 2008, **10**(44), 6615–6620.

42 *RStudio, Integrated Development Environment for R, version 1.1.442*, RStudio, Inc., Boston, MA, 2016.

43 A. Kassambara and F. Mundt, *factoextra: Extract and Visualize the Results of Multivariate Data Analyses*, 2017. https://CRAN.R-project.org/package=factoextra, accessed June 28, 2018.

44 F. Chollet, *Keras*, 2015, https://keras.io, accessed June 20, 2018.

45 D. P. Kingma and J. Ba, Adam: A method for stochastic optimization, 2014, arXiv:1412.6980. arXiv.org e-Print archive, https://arxiv.org/abs/1412.6980, accessed June 20, 2018.

46 F. V. G. Pedregosa, A. Gramfort, V. Michel, B. Thirion, O. Grisel, M. Blondel, P. Prettenhofer, R. Weiss, V. Dubourg, J. Vanderplas, A. Passos, D. Cournapeau, M. Brucher, M. Perrot and E. Duchesnay, Scikit-learn: Machine Learning in Python, *J. Mach. Learn. Res.*, 2011, **12**, 2825–2830.

47 C. E. Rasmussen and C. K. I. Williams, *Gaussian Processes for Machine Learning*, MIT Press, 2006.

48 H. Akaike, A New Look at the Statistical Model Identification, *IEEE Trans. Autom. Control*, 1974, **19**, 716–723.

49 G. Schwarz, Estimating the Dimension of a Model, *Ann. Stat.*, 1978, **6**(2), 461–464.